Accurate simulation of delamination under mixed-mode loading using a multilinear cohesive law

Abdel-Monsef, S.; Tijs, B. H.A.H.; Renart, J.; Turon, A.

DOI
10.1016/j.engfracmech.2023.109233

Publication date
2023

Document Version
Final published version

Published in
Engineering Fracture Mechanics

Engineering Fracture Mechanics 284 (2023) 109233

Contents lists available at ScienceDirect

Engineering Fracture Mechanics

journal homepage: www.elsevier.com/locate/engfracmech

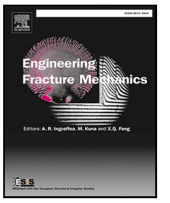

Accurate simulation of delamination under mixed-mode loading using a multilinear cohesive law

S. Abdel-Monsef [b], B.H.A.H. Tijs [c,d], J. Renart [a], A. Turon [a,*]

[a] University of Girona, AMADE, Polytechnic School, Girona, Spain
[b] Zagazig University, Faculty of Engineering, Zagazig, Egypt
[c] Fokker/GKN Aerospace, Papendrecht, The Netherlands
[d] Delft University of Technology, Faculty of Aerospace Engineering, Delft, The Netherlands

ARTICLE INFO

Keywords:
Delamination
Cohesive zone model
Cohesive law
Fracture
FEM
R-curve

ABSTRACT

The complex failure mechanisms involved in failure of interfaces requires the use of an accurate description of the cohesive law. In recent years, there have been many developments to determine the full shape of the cohesive law. However, most of the existing cohesive zone models assume a simplified shape, such as bilinear, trapezoidal or exponential, which are usually simple to model. Their accuracy is found to be rather limited, especially in the presence of a large fracture process zone due to either plastic deformation or fibre bridging. In this work, a new cohesive element description is proposed to formulate a general cohesive zone model to overcome these limitations. The benefit of the new approach is that it allows for convenient implementation of any arbitrary shape of the cohesive law obtained experimentally. The authors present a new procedure based on the superposition of n-bilinear cohesive zones to obtain an equivalent multilinear cohesive law that fits any experimental measurement. The new element formulation has been implemented in the commercial finite element software ABAQUS, using user element subroutine. Verification of the methodology is performed at the single element level and the approach is validated for different material systems (adhesives and composites) using the double cantilever beam, end-notched flexure and mixed-mode bending tests. Excellent correlation between all numerical predictions and experimental results is obtained, demonstrating the robustness of the proposed methodology.

1. Introduction

In the framework of finite element analyses, cohesive zone modelling is a powerful tool to simulate interfacial debonding and delamination analyses having the ability to model both crack initiation and propagation [1–9]. Accurate simulation of delamination is also important when predicting the detailed failure modes of composites, as they are generally governed by a complex interaction between ply splits and delaminations as shown by Tijs et al. [10].

The Cohesive Zone Model (CZM) has become a popular approach to accurately simulate the fracture process of interfaces [11,12]. The CZM method relates the cohesive stress to the displacement jumps along a damage length at an interface where a crack may initiate. The cohesive law of the element governs the softening behaviour and influences the development of the Fracture Process Zone (FPZ). The principle is as follows: (1) the elements initially behave linearly according to their penalty stiffness; (2) at a specific traction stress, damage initiates and starts the softening process; (3) during softening, the element stiffness is gradually damaged

* Corresponding author.
E-mail address: albert.turon@udg.edu (A. Turon).

https://doi.org/10.1016/j.engfracmech.2023.109233
Received 5 December 2022; Received in revised form 23 February 2023; Accepted 25 March 2023
Available online 5 April 2023

while dissipating energy according to a given fracture energy; (4) a new crack surface is formed when the stiffness and the strength are fully degraded and complete separation is obtained [13]. The initiation strength, fracture toughness and shape typically have to be determined experimentally and are different for the three opening modes: mode I (in the normal direction), shear mode II (in-plane direction) and mode III (out-of-plane direction), and mixed-mode. Different shapes of cohesive laws have been purposed in literature and applied for simulation of debonding and delamination in composite structures. Cohesive laws can be determined using direct methods that rely on experimental measurements of the traction separation law parameters, however, this is difficult to perform [14]. On the other hand, the cohesive law can also be calculated analytically or semi-analytically by using an inverse method [15,16]. The existing cohesive zone models in literature are formulated using various idealized shapes of the cohesive law, e.g. bilinear [4,11], trapezoidal [6] and exponential [17]. The above mentioned shapes are typically simple to model, however, their accuracy is found to be rather limited, especially in the presence of a large fracture process zone due to either plastic deformation or fibre bridging. In order to solve this, Sorensen et al. [18] combined a bilinear traction separation relation with an exponentially decaying function to represent the bridging effect. Airoldi and Dávila [19] and Tamuzs et al. [20] used a cohesive trilinear law to provide a simple linear description of the bridging. Furthermore, Dávila et al. [21] showed that bilinear softening provided a better approximation of the experimental R-curve during fracture of composites. Following the microscopic mechanism of delamination failure, Gong et al. [22] and Yin et al. [23] modified the method to represent quasi-brittle matrix failure and fibre bridging by assuming that the displacement at damage onset of fibre bridging is the same as the complete failure displacement for matrix failure. However, the mixed-mode tractions and separations leading to a particular cohesive law were not described, and this method required a genetic algorithm to determine the most suitable softening parameters. Jensen et al. [24] formulated a constitutive model based on a multilinear cohesive law with an arbitrary number of line segments. In this approach, the same Mixed-Mode interpolation between Mode I and Mode II components was selected for all the line segments and the pure mode cohesive laws were obtained by an optimization process to fit the numerical response to the experimental data of an specimen loaded with uneven moments. Tijs et al. [25] used a cohesive law in tabular form to describe fibre bridging in thermoplastic composites using the built-in Abaqus cohesive element, which requires an user-defined interpolated cohesive law. In Tijs et al. [25], the pure mode cohesive laws were obtained from an inverse procedure and the influence of the dependence of the different failure mechanisms with the mode mixity was investigated. De Carvalho et al. [26] proposed a cohesive element using a piecewise-linear cohesive law assuming different shapes for mode I and II to account for different failure mechanisms. The measured cohesive law is scaled differently for mode I and II to avoid artificial damage/healing during mixed-mode loading. The concept of generalized piecewise-linear cohesive laws can also be adopted to take into account the failure mechanisms caused by the fibrillation of soft adhesive layers and the variation of the peel angle considering the shear flow mechanism that influence the mixed-mode behaviour [27]. Therefore, there is a need of defining a general cohesive law that can be adapted to the experimental measurements, with a straigh-forward model parameter identification, and also able to independently deal with the mixed-mode interpolation of the different failure mechanisms. Compared to the above mentioned works, the benefit of the proposed methodology is that it allows for a straight-forward parameter identification process and mixed-mode interaction can be defined on the individual line segments, which makes it possible to treat individually each failure mode that contributes to the cohesive law.

In the current work, the constitutive model by Turon et al. [11] is further developed to account for softening using a MultiLinear Cohesive Law (MLCL) with an arbitrary number of line segments that can fit any experimentally measured cohesive law. The constitutive model is implemented in the commercial Finite element software ABAQUS using the user element subroutine. The numerical model is first verified on several single element tests and validated on a number of fracture toughness tests from the available experimental work on adhesives by Sarrado et al. [14] and thermoplastic composites by Tijs et al. [25].

2. Formulation of the multilinear cohesive zone model

The formulation of the multilinear cohesive zone model is described in more detail in this section. The procedure is based on the same interface kinematics as described by Turon et al. [11], where the model is further developed to solve problems that require the use of a complex shape of the traction-separation law.

2.1. Multilinear cohesive law

The multilinear shape of the traction separation law, with an arbitrary number of line segments (NCL), can be simplified, employing the principle of superposition [21] of bilinear traction separation laws, as shown in Fig. 1:

$$\tau_j(\Delta_j) = \sum_{i=1}^{i=n-1} K_{j(i)}(1 - D_{j(i)})\Delta_j \tag{1}$$

where τ_j and Δ_j are the traction stress and the displacement jump for a certain loading mode $j = I, II, III$, respectively. For an arbitrary bilinear traction separation law, $K_{j(i)}$ is the equivalent stiffness and $D_{j(i)}$ is the damage parameter associated with loading mode j and the bilinear cohesive law number i ($i = 1, 2, 3, \ldots, \mathrm{n} - 1$; where n is the end-point of the MLCL as shown in Fig. 1).

Each bilinear cohesive law can be defined using three parameters: the onset traction stress $\tau^o_{j(i)}$, the initiation and the critical displacement jumps ($\Delta^o_{j(i)}$ and $\Delta^c_{j(i)}$). Each of these parameters can be defined using the process summarized in Fig. 2 where any shape of the cohesive law can be transformed into a series of bi-linear cohesive laws. Firstly, it is considered that the two end-points of the last segment of the MLCL composes of the softening part of the last bi-linear cohesive law (see Fig. 2-b where i = n − 1) and the onset traction stress $\tau^o_{j(n-1)}$ of the last bi-linear cohesive law is equal to the traction stress $\tau_{(n-1)}$ of the MLCL. For clarity, the

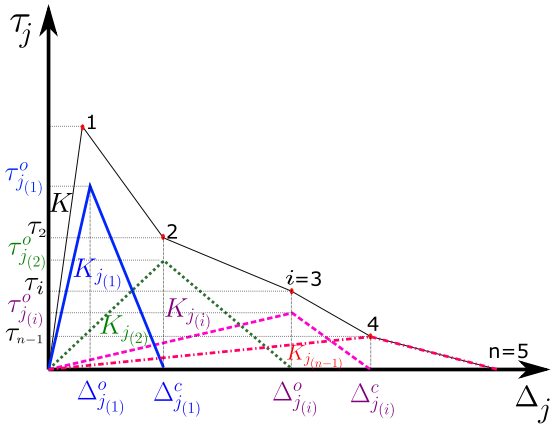

Fig. 1. A mixed-mode multilinear cohesive law.

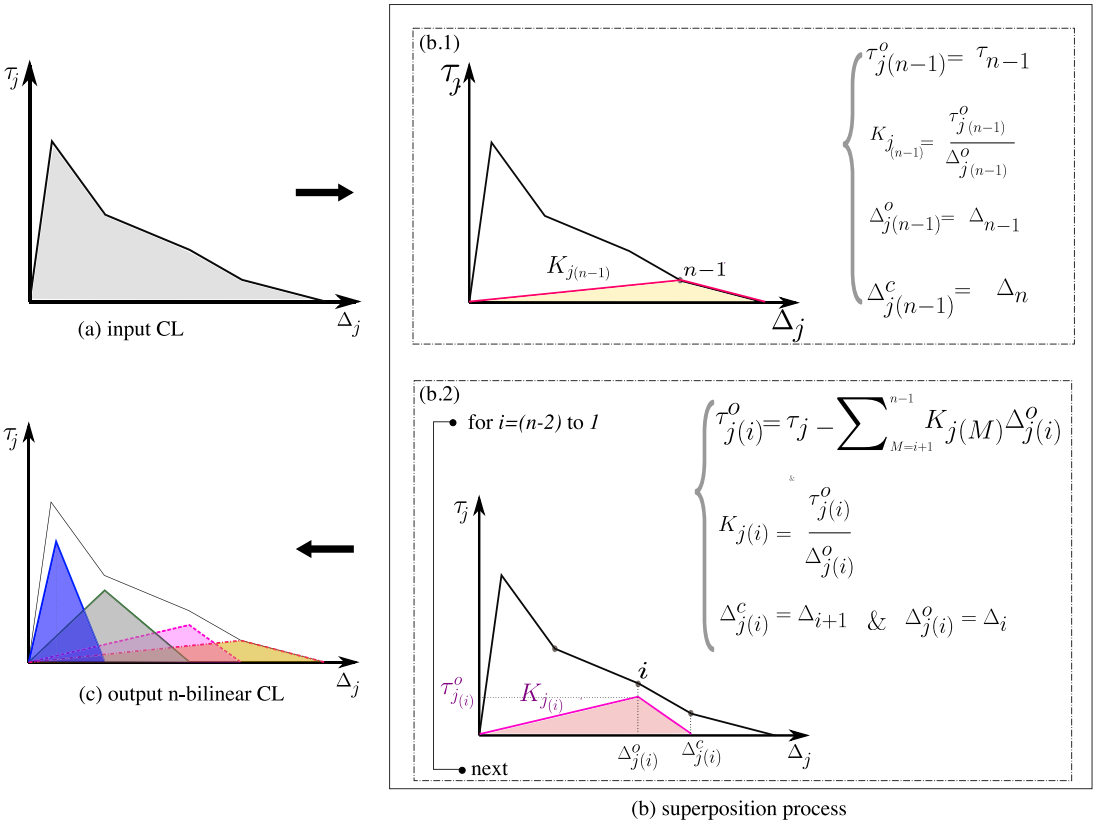

Fig. 2. A procedure of superposing of multilinear cohesive law into n-bilinear cohesive laws where (a) the input multilinear CL, (b) the superposition process and (c) the output n-bilinear cohesive laws.

process is initiated by assembling the bi-linear cohesive laws from the last segment to the first one of the input multilinear cohesive law.

Once the last bilinear cohesive law is defined, a systematic procedure can be performed using Eqs. (2) and (3) (see Fig. 2-b). The displacement jumps at the two end-points of each segment in the MLCL are the initiation and the critical displacement jump (Δ^o and Δ^c) in the associated bilinear cohesive law. Where subindex i refers to the MLCL point and the $i-1$ number of the bilinear cohesive law, being n the total number of points and NCL $= n-1$ the total number of cohesive laws. Finally, $\Delta^c_{j(i)} = \Delta^o_{j(i+1)}$ and the

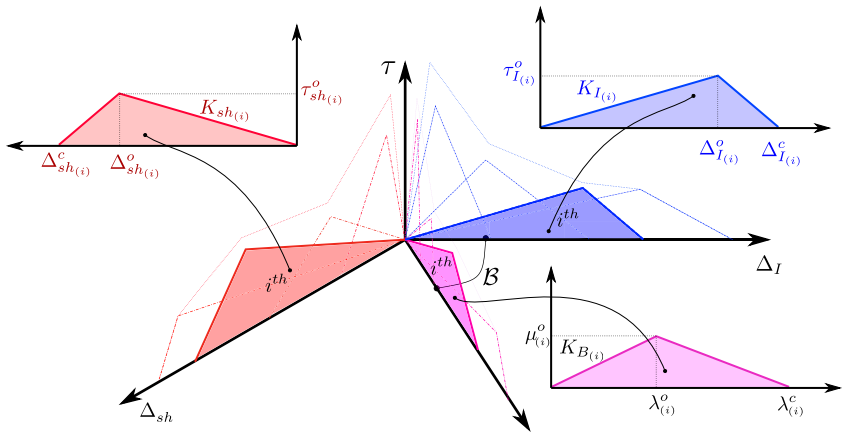

Fig. 3. The equivalent mixed-mode series of bilinear cohesive laws.

onset traction stress can be defined using the following equations:

$$\tau_j = \tau^o_{j(i)} + \sum_{M=i+1}^{n-1} K_{j(M)} \Delta^o_{j(i)} \tag{2}$$

$$K_{j(i)} = \frac{\tau^o_{j(i)}}{\Delta^o_{j(i)}} \tag{3}$$

2.2. Damage model and mixed-mode interpolation

Moving to the interaction between these bilinear cohesive laws to form the damage model, the mixed-mode displacement jump (λ) can be defined as [11]:

$$\lambda = \frac{K_I \langle \Delta_I \rangle^2 + K_{sh} \Delta^2_{sh}}{\sqrt{K^2_I \langle \Delta_I \rangle^2 + K^2_{sh} \Delta^2_{sh}}} \quad ; \quad \Delta_{sh} = \sqrt{\Delta^2_{II} + \Delta^2_{III}} \tag{4}$$

where K_j and Δ_j are the mode dependent penalty stiffness and the displacement jumps at the integration points for a certain loading mode, $j = I, II, III$. For convenience, subindex $j = I$ for mode I loading and $j = sh$ for shear loading (combination of modes II and III). The $\langle \bullet \rangle$ is the Macaulay bracket defined as $\langle x \rangle = \frac{1}{2}(x + |x|)$. The local degree of mixed-mode ratio (B) is computed pointwise at every finite element integration point [4,11]:

$$B = \frac{K_{sh} \Delta^2_{sh}}{K_I \langle \Delta_I \rangle^2 + K_{sh} \Delta^2_{sh}} \tag{5}$$

There is one equivalent mixed-mode cohesive law for a given set of pure mode cohesive laws and a mixed-mode ratio. This mixed-mode cohesive law can be transformed into a series of mixed-mode bilinear cohesive laws (see Fig. 3). For each ith pair of pure mode cohesive law, the mixed-mode variables ($\lambda^o_{(i)}$ and $\lambda^c_{(i)}$) can be associated with the ith cohesive law (see Fig. 4). $\lambda^o_{(i)}$ and $\lambda^c_{(i)}$ are the dummy mixed-mode onset, and critical displacement jumps for the selected bilinear cohesive law, which can be defined using Benzeggagh–Kenane [28] as mixed-mode interaction:

$$\lambda^o_{(i)} = \sqrt{\frac{K_{I(i)} (\Delta^o_{I(i)})^2 + [K_{sh(i)} (\Delta^o_{sh(i)})^2 - K_{I(i)} (\Delta^o_{I(i)})^2] B^{\eta_i}}{K_{B(i)}}} \tag{6}$$

$$\lambda^c_{(i)} = \frac{K_{I(i)} \Delta^o_{I(i)} \Delta^c_{I(i)} + [K_{sh_{(i)}} \Delta^o_{sh(i)} \Delta^c_{sh(i)} - K_{I(i)} \Delta^o_{I(i)} \Delta^c_{I(i)}] B^{\eta_i}}{K_{B(i)} \lambda^o_{(i)}} \tag{7}$$

where $\Delta^o_{I(i)}$, $\Delta^o_{sh(i)}$ are the onset displacement jumps, and $\Delta^c_{I(i)}$, $\Delta^c_{sh(i)}$ are the critical displacement jumps, respectively. Subindexs $\bullet_{I(i)}$ and $\bullet_{sh(i)}$ refer to the mode I and the shear mode of loading, while (i) is the order in the series of the bilinear cohesive laws. $K_{B_{(i)}}$ is the equivalent penality stiffness associated with the ith cohesive law:

$$K_{B(i)} = K_{I(i)}(1 - B) + K_{sh(i)} B \tag{8}$$

During the failure process, different failure mechanisms develop depending on the mode mixity (and the material system) and can result in large fracture process zones (for example due to fibre bridging) that significantly change from opening to shear mode loading. Then, the mixed mode interpolation becomes tricky [25] and can also result in an unequal number of line segments for pure

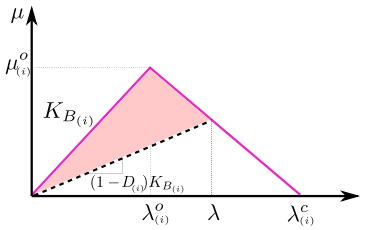

Fig. 4. Representation of the ith bilinear cohesive law used in the formulation for a fixed mode ratio. $\mu^o_{(i)}$ is the onset stress.

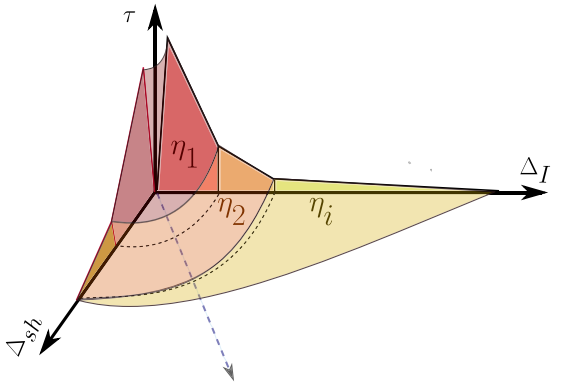

Fig. 5. Sketch of mixed-mode interpolation of two different number of line segments of cohesive laws.

mode cohesive laws. The formulation presented above is, in these sense, very flexible: each bilinear cohesive law or line segment can be associated with a different damage mechanism and the mixed mode interpolation can be dealt independently, defining a different BK parameter (η_i) for each bilinear cohesive law. For example, Fig. 5 represent the mixed mode interpolation between a 3-segment mode I cohesive law and a 2-segment mode II cohesive law. The reason for such kind of interpolation can be in the presence of extensive fibre bridging, which does not play a role in mode II. Therefore, the last segment goes from the mode I "fibre bridging toughness" to a mode II fracture toughness of zero. Furthermore, the BK parameter η_i of each segment can also be adjusted to control the interpolation. (see Fig. 4).

The damage activation function presented in [11] is used locally for each mixed-mode bilinear constitutive law where a $2n$ state variable is used to store the associated threshold function $r_{\mathcal{D}_{(i)}}$. For the ith bilinear cohesive law, the local damage activation function reads:

$$\mathcal{F}_{(i)}(\lambda) = \mathcal{L}_{(i)}(\lambda) - r_{\mathcal{D}_{(i)}} \leq 0 \tag{9}$$

where $\mathcal{L}_{(i)}(\lambda)$ is the local monotonic loading function that is updated at every time t increment of the analysis. Both of $\mathcal{L}_{(i)}(\lambda)$ and the local damage activation function $r_{\mathcal{D}_{(i)}}$ can be defined as:

$$\mathcal{L}_{(i)}(\lambda) = min\left\{\frac{\lambda - \lambda^o_{(i)}}{\lambda^c_{(i)} - \lambda^o_{(i)}}, 1\right\} \tag{10}$$

$$r_{\mathcal{D}_{(i)}} = max\{0, \underset{s}{max}[\mathcal{L}_{(i)}(\lambda)]\} \qquad 0 < s < t \qquad \forall t \tag{11}$$

Finally, to complete the definition of the constitutive model, a global damage variable, $\mathcal{D}$, should be defined, which is used to define the constitutive tangent tensor:

$$(1-D)K_B = \sum_{i=1}^{i=n-1}\left[1 - \frac{r_{\mathcal{D}_{(i)}}\lambda^c_{(i)}}{r_{\mathcal{D}_{(i)}}\lambda^c_{(i)} + (1 - r_{\mathcal{D}_{(i)}})\lambda^o_{(i)}}\right]K_{B(i)} \tag{12}$$

where K_B is the equivalent penalty stiffness of the mixed-mode MLCL which can be decomposed using the following superposition:

$$K_B = \sum_{i=1}^{i=n-1} K_{B(i)} \tag{13}$$

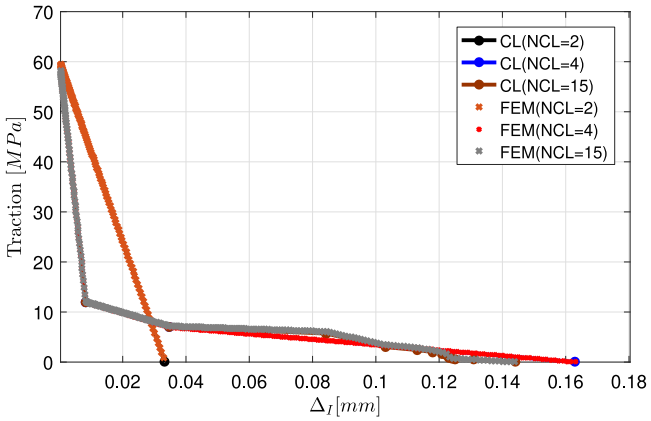

Fig. 6. The numerical results of using three different shapes of cohesive law.

3. Verification of methodology

In order to verify the aforementioned formulation, different finite element models, consisting of a single user element, have been used. First, three different FE models have been constructed using cohesive laws consisting of different number of line-segments to demonstrate the capability of the new formulation. And then, the mixed-mode interpolation has been verified using a MLCL shape for both mode I and mode II.

The MLCL formulation presented in the previous section has been implemented in ABAQUS [29] as a user-written element subroutine (UEL). The lower surface of the single element is fixed while the upper surface is subjected to predefined displacements U_X and U_Z, which represent the shear displacement jumps Δ_{shear} and the separation opening displacement Δ_I, respectively. The general loading mode can be defined by applying the displacement U_m and the loading angle θ which corresponds to the mixed-mode ratio. Angle θ is defined in radians ranging from 0 to 1 (Mode I: 0, Mode II: 1). Therefore, U_X and U_Z can be defined as:

$$U_X = U_m \sin(\theta) \quad ; \quad U_Z = U_m \cos(\theta) \tag{14}$$

Three different shapes of cohesive laws (NCL = 2, 4 and 15) that have the same fracture toughness, onset traction stress and penalty stiffness have been modelled, see Fig. 6. The CLs obtained from the simulations have been compared to the predefined ones. The new formulation is capable of modelling the different shapes of cohesive laws, ranging from bi-linear shape to more complex shapes, as shown in Fig. 6 where the output of the simulations lies on top of the input cohesive laws.

To this point, the procedure is capable of modelling the nonlinear shape of the cohesive law. Moreover, to clarify how the mixed-mode interpolation works, FE models have been constructed using an arbitrary shape of cohesive law consisting of 15 line segments for both mode I and mode II, see Fig. 7. The area under the cohesive laws represents the fracture toughness value (G_{Ic} = 0.45 N/mm, G_{IIc} = 1.85 N/mm) for mode I and mode II respectively. The single user element FE model has been run with the boundary conditions defined to ensure a constant mixed mode ratio of 50% and 75%, respectively. As can be seen in Fig. 7, the input cohesive laws are solid lines while the resulting nodal force–displacement curves obtained from the user element model are plotted in dashed lines for both mixed-mode ratios of 50% and 75%. The areas under the output nodal force–displacement curves are perfectly equal to the calculated fracture toughness using Benzeggagh–Kenane (η_i = 2) for both mixed-mode ratios. Moreover, the present formulation works in the case of more complex shapes of mixed-mode cohesive laws as shown in Fig. 7.

4. Numerical analyses

In this section, the MLCL formulation is validated on a number of fracture toughness tests from the available experimental work on composite bonded joints (adhesives) by Sarrado et al. [14] and thermoplastic composites by Tijs et al. [25].

4.1. Analysis of bonded joints

Three different bonded joints configurations found in [14], Double Cantilever Beam (DCB), End Notched Flexure (ENF) and Mixed Mode Bending (MMB) 50%, were simulated using the commercial software ABAQUS [29]. The geometry and properties of the specimens (named A2T2) were taken from Ref. [14]. The arms of the specimens were 250 mm long, 25 mm wide and 2.2 mm thick (the two T800S/M21 carbon/epoxy adherends were co-bonded using two layers of the FM-300 adhesive layer with an insert length of 60 mm). The elastic properties of the adherends are listed in Table 1. For a more detailed explanation of the specimen configurations, the reader should refer to [14].

The finite element models were performed using 2D plane strain CPE4I elements for the adherends, connected using 4-node cohesive elements along the crack path. Five elements were used in the thickness direction for each adherend, and the element

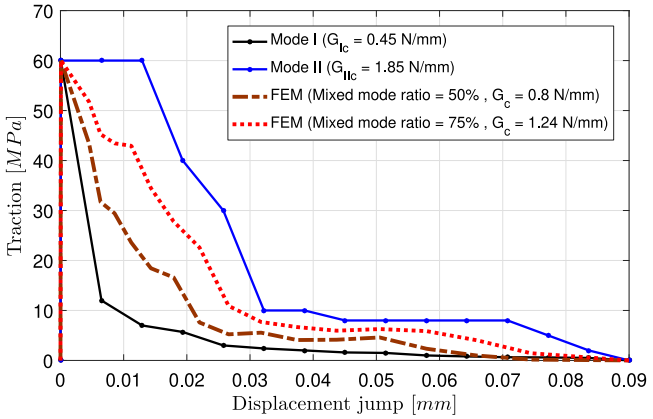

Fig. 7. The numerical results for mixed-mode ratios of 50% and 75%.

Table 1
Elastic properties of the adherends.

E_{11}	$E_{22} = E_{33}$	$G_{12} = G_{13}$	G_{23}	$\nu_{12} = \nu_{13}$	ν_{23}
142.0 GPa	7.80 GPa	4.00 GPa	2.80 GPa	0.34	0.40

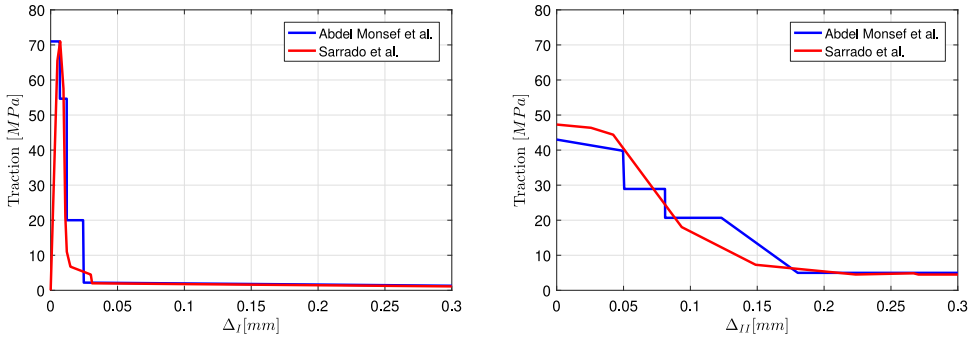

Fig. 8. The cohesive laws of A2T2 specimens [14] for Mode I and Mode II.

length was set to 0.1 mm in the longitudinal direction. Two different methods were used to obtain the cohesive laws. The first one is an experimental method used by Sarrado et al. [14] while the second one is semi-analytical method (called inverse method [15,16]) that extract the cohesive law from only the load–displacement curve for each of the mode I and mode II test configurations. Fig. 8 shows the extracted cohesive law plotted together with the softening part of the experimental cohesive law.

A comparison among the experimental results and the finite element model behaviour using the specimen A2T2 is plotted in Fig. 9. The numerical load–displacement curves obtained using bilinear cohesive law show an overestimation of the peak load with respect to the experimental response, in addition to some difference between the numerical load–displacement curve and the experimental response. Therefore, the bilinear cohesive law is not enough to simulate the studied bonded joints. On the other hand, applying the new approach using the MLCL gives an excellent agreement with the experimental load–displacement curves in [14] as shown in Fig. 9.

The new MLCL methodology can simulate a bonded joint using a mixed-mode MLCL with an arbitrary number of line segments from the results mentioned above. Nevertheless, what happens if a bilinear cohesive law is used? To answer this question, four different cohesive laws are selected while using the same fracture toughness and maximum traction stress. A comparison of the four different cohesive laws is shown in Fig. 10(b). The obtained numerical results in Fig. 10(a) show that using a bilinear cohesive law predicts a different response and leads to an overestimation of the peak load. As the number of the cohesive law segment lines increases, the accuracy of the simulation also improves. This demonstrates the importance of accounting for an accurate shape of the cohesive law in the simulation of interfaces.

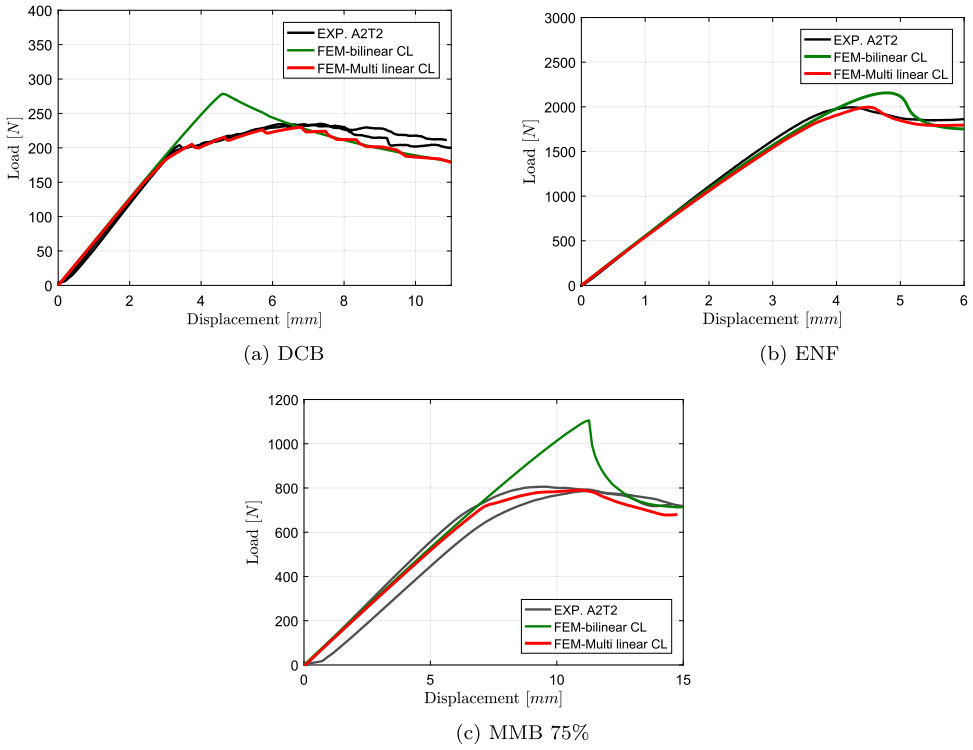

Fig. 9. Experimental [14] and numerical load–displacement curves of the (a) DCB, (b) ENF, and (c) MMB 75% tests.

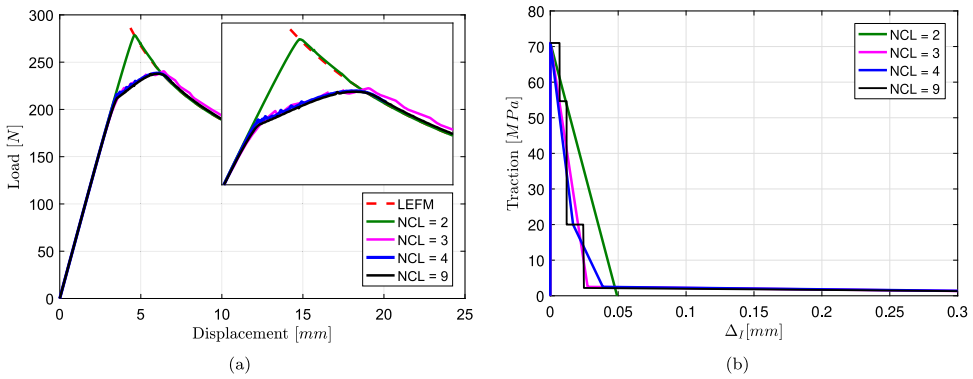

Fig. 10. Numerical analysis of A2T2 specimen [14]: (a) For different load–displacement curves (b) four different cohesive laws based on same fracture energy and maximum traction stress.

Table 2
AS4D/PEKK-FC thermoplastic composite elastic properties [25,30].

E_{11}	$E_{22} = E_{33}$	$G_{12} = G_{13}$	G_{23}	$\nu_{12} = \nu_{13}$	ν_{23}
133.15 GPa	10.95 GPa	5.19 GPa	3.50 GPa	0.316	0.487

4.2. Analysis of interlaminar fibre bridging of thermoplastic composites

The MLCL methodology is further evaluated by analysing the interlaminar behaviour of thermoplastic composites. The Double Cantilever Beam (DCB) results presented in Tijs et al. [25] show a dominant effect of fibre bridging, which is highly influencing the interlaminar behaviour. The AS4D/PEKK-FC thermoplastic composite material properties are given in Table 2. For the longitudinal and transverse modulus, the average of tension and compression is presented.

The DCB test is performed following the ISO 15024 test standard [31]. Side-clamp beam [32] hinges are used to load the specimens with an initial crack length of $a_0 = 48$ mm. The experimental load–displacement curve of the DCB test is shown in

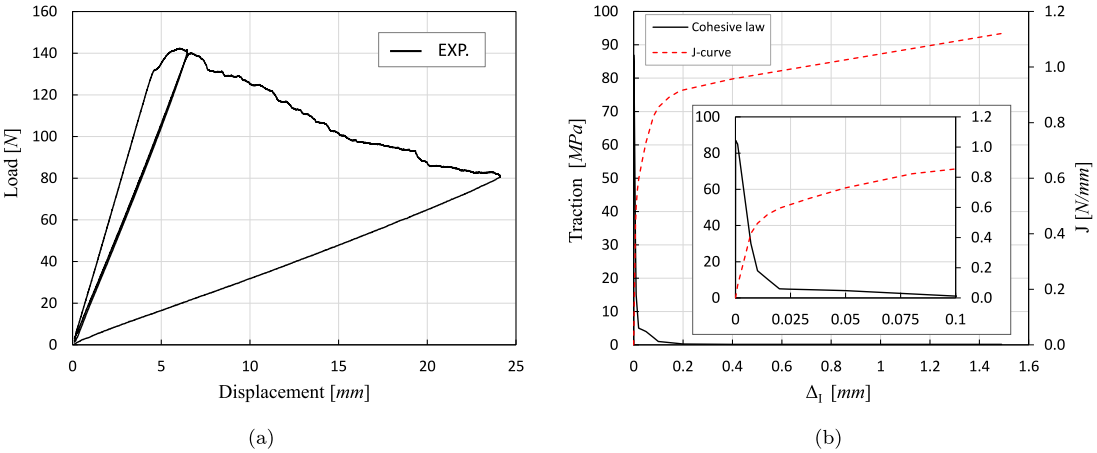

Fig. 11. Interlaminar experimental data thermoplastic composites from [25]: (a) load–displacement curves of DCB test; (b) the associated cohesive law and J-curve.

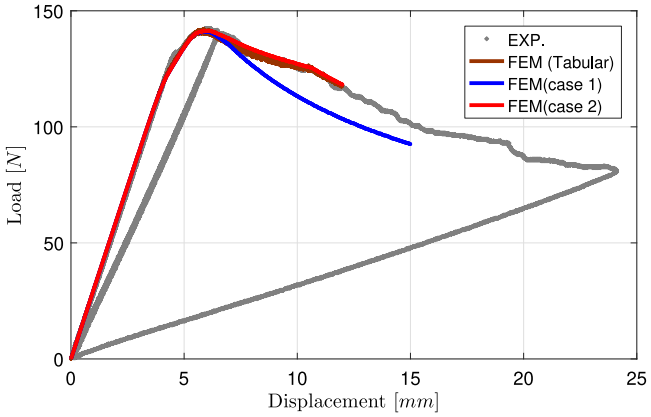

Fig. 12. Comparison of numerical TABULAR and MLCL to experimental results of DCB test from Tijs et al. [25].

Fig. 11(a) and the corresponding numerical cohesive law and J-curve are shown in Fig. 11(b). As can be observed in Fig. 11, fibre bridging highly influences the interlaminar fracture toughness and this results in a long tail in the cohesive law and corresponding J-curve. The shape at the start of the cohesive law and J-curve is also shown in more detail in Fig. 11(b).

The analysis results using the MLCL methodology are compared against the experimental and numerical results presented in [25], this is shown in Fig. 12. A tabular cohesive law (named FEM(tabular)) is defined using the procedure described in [25] that allows for an accurate description of the cohesive law in the ABAQUS finite element software. Tijs et al. [25] demonstrated that this is especially important when a high penalty stiffness is used or when sudden changes in the shape of the cohesive law are present.

The comparison in Fig. 12 shows an excellent agreement between the experimental and numerical tabular cohesive law. The same level of correlation can be achieved by making use of the MLCL (named as FEM(case 2)). However, it is not the case for the cohesive law without fibre bridging (FEM(case 1)), see Fig. 12. Including or removing the fibre bridging effect in the MLCL methodology is easily achieved by adjusting only the cohesive law that is responsible for the tail of the traction-separation law.

The experimental data reported by Tijs et al. [25] has been used to demonstrate the capability of the proposed methodology to model the influence of fibre bridging of thermoplastic composites subjected to mixed-mode loading conditions. As reported by Tijs et al. [25], no fibre bridging was observed during the MMB 50% test, but it has a dominant influence in mode I.

Fig. 13-a shows the interpolation of the multilinear cohesive law. Mode I and mode II have a different number of line segments and different values for the BK-parameter (η_1 and η_2) associated with individual failure mechanism. η_1 represents the BK-parameter for the first two segments while η_2 is used for the last segment. The fibre bridging effect is associated to the tail or third segment of the mode I cohesive law. Different values of η_1 and η_2 have been selected to show the influence of the mixed mode interpolation on the results. The first selection is $\eta_1 = \eta_2 = 2.9$ which is the value reported in Tijs et al. [25]. However, as discussed in Tijs et al. [25], if the fibre bridging effect is disregarded, then $\eta = 2.1$. Therefore, η_1 has been ranged from 2.9 to 2.1 and the corresponding η_2 value has been computed to obtain a total mixed mode fracture toughness for $B = 0.5$ equal to 1.27 N/mm, the value reported in Tijs et al. [25]. The dependence of the mixed-mode fracture toughness on the different selection of (η_1, η_2) is shown in Fig. 13-b.

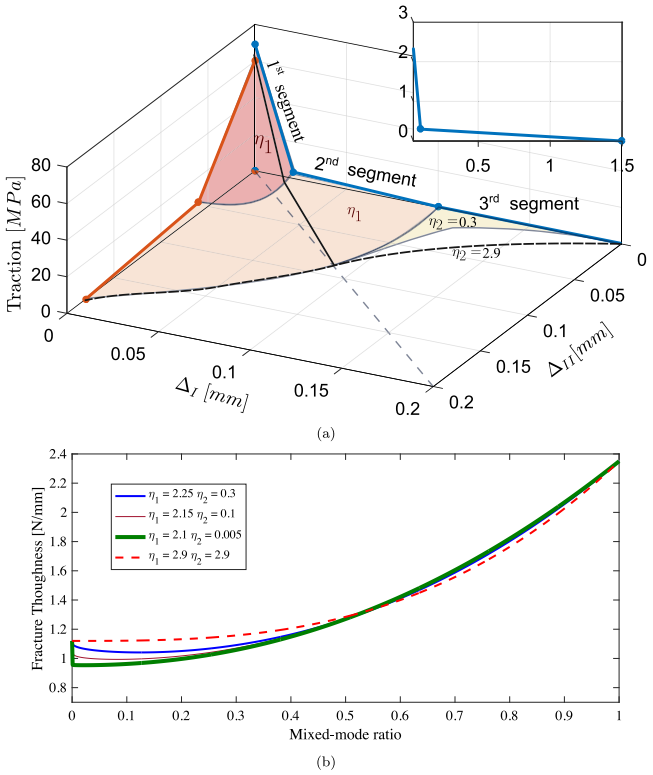

Fig. 13. Mixed mode interpolation of mode I and mode II cohesive law.

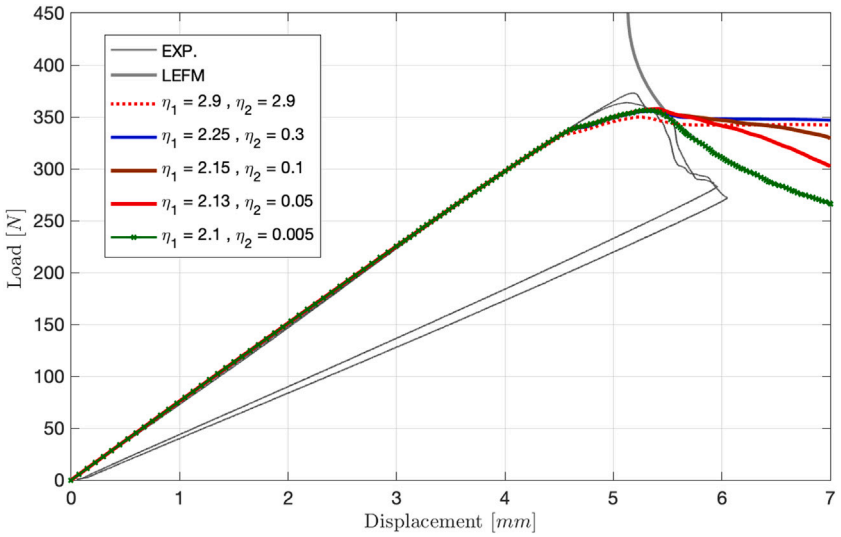

Fig. 14. Comparison of numerical MLCL to experimental results of MMB 50% test from Tijs et al. [25].

It can be observed that for lower mode mixities the influence of the third segment of the mode I cohesive law strongly depends on the selection of η_2. The limit case, $\eta_2 = 0$, supress the fibre bridging effect if there is a mode II displacement component. The influence of the selection of the (η_1, η_2) parameters on the load–displacement curve of a mixed-mode bending test with $B = 50\%$ is shown in Fig. 14. The numerical results are compared to the experimental data from Tijs et al. [25] and the Linear Elastic Fracture Mechanics (LEFM) curve. For η_1 and η_2 is equal to 2.9 a large mismatch between the numerical and the experimental propagation is obtained. When decreasing the value of η_2, the numerical prediction approaches the LEFM solution. If the fibre bridging effect is

limited to almost pure mode I loading ($\eta_2 = 0.005$), then a good agreement between the numerical and the analytical responses is obtained .

5. Conclusions

A new MLCL formulation for cohesive elements has been successfully developed that can describe the complex failure mechanisms involved in failure of interfaces. The methodology is verified on the single element level and validated for metal bonded joints (adhesives) and delamination in composites. It is shown that the MLCL formulation can adapt to complex shapes to match the failure behaviour such as fibre bridging observed experimentally. The original formulation, [4,11], was limited to the bilinear shape of cohesive law while the current version is based on the superposition of n-bilinear cohesive zone to produce an equivalent MLCL with an arbitrary number of line-segments. One of the benefits of the proposed methodology is that it allows for a straightforward parameter identification process and mixed-mode interaction can be defined on the individual line segments, which makes it possible to treat each failure mode that contributes to the cohesive law individually. Validation of the methodology shows excellent correlation between numerical predictions and experimental results, demonstrating that the methodology provides an accurate solution for the simulation of delamination and damage in interfaces.

CRediT authorship contribution statement

S. Abdel-Monsef: Writing – original draft, Validation, Software, Methodology, Formal analysis, Conceptualization. **B.H.A.H. Tijs:** Writing – review & editing, Validation, Methodology, Investigation, Formal analysis, Conceptualization. **J. Renart:** Writing – review & editing, Validation, Supervision, Funding acquisition. **A. Turon:** Writing – review & editing, Supervision, Methodology, Funding acquisition, Formal analysis, Conceptualization.

Declaration of competing interest

The authors declare the following financial interests/personal relationships which may be considered as potential competing interests: Albert Turon reports financial support was provided by Spain Ministry of Science and Innovation. Bas Tijs reports financial support was provided by European Commission. Jordi Renart reports financial support was provided by Spain Ministry of Science and Innovation.

Data availability

Data will be made available on request.

Acknowledgements

This work has been partially funded by the Spanish Government (Ministerio de Ciencia e Innovación) under contract PID2021-127879OB-C21.

The second author received co-funding from the Clean Sky 2 Joint Undertaking (JU) under grant agreement No 945583 (project STUNNING). The JU receives support from the European Union's Horizon 2020 research and innovation programme and the Clean Sky 2 JU members other than the Union. The second author also acknowledges the Fokker/GKN Aerospace COMPFRAC and THOR project that supported these developments.

References

[1] Blackman B, Hadavinia H, Kinloch AJ, Williams J. The use of a cohesive zone model to study the fracture of fibre composites and adhesively-bonded joints. Int J Fract 2003;119(1):25–46.
[2] Campilho RD, Banea MD, Neto J, da Silva LF. Modelling adhesive joints with cohesive zone models: effect of the cohesive law shape of the adhesive layer. Int J Adhes Adhes 2013;44:48–56.
[3] Noorman D. Cohesive zone modelling in adhesively bonded joints: Analysis on crack propagation in adhesives and adherends (Master's thesis), Technical University of Delft; 2014.
[4] Turon A, Camanho PP, Costa J, Dávila C. A damage model for the simulation of delamination in advanced composites under variable-mode loading. Mech Mater 2006;38(11):1072–89.
[5] Jumel J, Salem NB, Budzik MK, Shanahan ME. Measurement of interface cohesive stresses and strains evolutions with combined mixed mode crack propagation test and backface strain monitoring measurements. Int J Solids Struct 2015;52:33–44.
[6] Tvergaard V, Hutchinson JW. The relation between crack growth resistance and fracture process parameters in elastic-plastic solids. J Mech Phys Solids 1992;40(6):1377–97.
[7] Tvergaard V, Hutchinson JW. The influence of plasticity on mixed mode interface toughness. J Mech Phys Solids 1993;41(6):1119–35.
[8] Tvergaard V, Hutchinson JW. On the toughness of ductile adhesive joints. J Mech Phys Solids 1996;44(5):789–800.
[9] Li S, Thouless M, Waas A, Schroeder J, Zavattieri P. Use of a cohesive-zone model to analyze the fracture of a fiber-reinforced polymer–matrix composite. Compos Sci Technol 2005;65(3–4):537–49.
[10] Tijs B, Dávila C, Turon A, Bisagni C. The importance of accounting for large deformation in continuum damage models in predicting matrix failure of composites. Composites A 2023;164:107263. http://dx.doi.org/10.1016/j.compositesa.2022.107263.
[11] Turon A, González E, Sarrado C, Guillamet G, Maimí P. Accurate simulation of delamination under mixed-mode loading using a cohesive model with a mode-dependent penalty stiffness. Compos Struct 2018;184:506–11.

[12] de Oliveira LA, Donadon MV. Delamination analysis using cohesive zone model: A discussion on traction-separation law and mixed-mode criteria. Eng Fract Mech 2020;228:106922.
[13] Pirondi A, Moroni F. Simulating fatigue failure in bonded composite joints using a modified cohesive zone model. In: Composite joints and connections. Elsevier; 2011, p. 363–98.
[14] Sarrado C, Turon A, Costa J, Renart J. An experimental analysis of the fracture behavior of composite bonded joints in terms of cohesive laws. Composites A 2016;90:234–42.
[15] Abdel Monsef S, Ortega A, Turon A, Maimí P, Renart J. An efficient method to extract a mode I cohesive law for bonded joints using the double cantilever beam test. Composites B 2019;178:107424.
[16] Abdel Monsef S, Pérez-Galmés M, Renart J, Turon A, Maimí P. The influence of mode II test configuration on the cohesive law of bonded joints. Compos Struct 2019;111689.
[17] Goyal VK, Johnson ER, Davila CG. Irreversible constitutive law for modeling the delamination process using interfacial surface discontinuities. Compos Struct 2004;65(3–4):289–305.
[18] Sorensen L, Botsis J, Gmür T, Humbert L. Bridging tractions in mode I delamination: Measurements and simulations. Compos Sci Technol 2008;68(12):2350–8.
[19] Airoldi A, Dávila CG. Identification of material parameters for modelling delamination in the presence of fibre bridging. Compos Struct 2012.
[20] Tamuzs V, Tarasovs S, Vilks U. Progressive delamination and fiber bridging modeling in double cantilever beam composite specimens. Eng Fract Mech 2001.
[21] Dávila CG, Rose CA, Camanho PP. A procedure for superposing linear cohesive laws to represent multiple damage mechanisms in the fracture of composites. Int J Fract 2009;158(2):211–23.
[22] Gong Y, Hou Y, Zhao L, Li W, Zhang J, Hu N. A modified mode I cohesive zone model for the delamination growth in DCB laminates with the effect of fiber bridging. Int J Mech Sci 2020;176:105514.
[23] Yin S, Gong Y, Li W, Zhao L, Zhang J, Hu N. A novel four-linear cohesive law for the delamination simulation in composite DCB laminates. Composites B 2020;180:107526.
[24] Jensen SM, Martos M, Bak BLV, Lindgaard E. Formulation of a mixed-mode multilinear cohesive zone law in an interface finite element for modelling delamination with R-curve effects. Compos Struct 2019;216:477–86.
[25] Tijs BHAH, Abdel-Monsef S, Renart J, Turon A, Bisagni C. Characterization and analysis of the interlaminar behavior of thermoplastic composites considering fiber bridging and R-curve effects. Composites A 2022;162:107101. http://dx.doi.org/10.1016/J.COMPOSITESA.2022.107101.
[26] De Carvalho N, Czabaj M, Ratcliffe J. Piecewise-linear generalizable cohesive element approach for simulating mixed-mode delamination. Eng Fract Mech 2021;242:107484.
[27] Yang Z, Xia Y, Yang F, Zhu Z, Sun Y, Jiang H. Peeling angle effect on soft adhesive: Mixed-mode CZM considering fibrillation. Eng Fract Mech 2022;274:108778.
[28] Benzeggagh ML, Kenane M. Measurement of mixed-mode delamination fracture toughness of unidirectional glass/epoxy composites with mixed-mode bending apparatus. Compos Sci Technol 1996;56(4):439–49.
[29] ABAQUS. ABAQUS 6.14 user's manual. 2014.
[30] Tijs B, Doldersum M, Turon A, Waleson J, Bisagni C. Experimental and numerical evaluation of conduction welded thermoplastic composite joints. Compos Struct 2021;114964. http://dx.doi.org/10.1016/J.COMPSTRUCT.2021.114964.
[31] ISO 15024:2001 fibre-reinforced plastic composites — Determination of mode I interlaminar fracture toughness, GIC, for unidirectionally reinforced materials. 2001.
[32] Renart J, Blanco N, Pajares E, Costa J, Lazcano S, Santacruz G. Side clamped beam (SCB) hinge system for delamination tests in beam-type composite specimens. Compos Sci Technol 2011;71(8). http://dx.doi.org/10.1016/j.compscitech.2010.10.005.